Available online at www.sciencedirect.com
ScienceDirect
Trans. Nonferrous Met. Soc. China 35(2025) 4217−4229
Transactions of Nonferrous Metals Society of China
www.tnmsc.cn

Enhancing long-term cycling stability of spinel $LiNi_{0.5}Mn_{1.5}O_4$ cathode via ultrathin ZrO_2 coating layer

Jie MEI[1,2], Qi-xiang XU[1,2], Yuan-zhi CHEN[1,2], Gui-yang GAO[1,2], Wan-jie XU[1,2], Qing-shui XIE[1,2], Lai-seng WANG[1,2], Dong-liang PENG[1,2]

1. State Key Laboratory of Physical Chemistry of Solid Surface, College of Materials, Xiamen University, Xiamen 361005, China;
2. Fujian Key Laboratory of Surface and Interface Engineering for High Performance Materials, Xiamen University, Xiamen 361005, China

Received 15 March 2024; accepted 11 December 2024

Abstract: Spinel $LiNi_{0.5}Mn_{1.5}O_4$ (LNMO) cathode draws significant attention in the field of energy storage due to its unique voltage plateau. To further enhance the long-term electrochemical stability of LNMO, the LNMO cathode covered with an ultrathin ZrO_2 layer was prepared through atomic layer deposition (ALD). It is found that the LNMO cathode deposited with 20 layers of ZrO_2 (LNMOZ20) exhibits the best electrochemical performance, achieving a high discharge capacity of 117.1 mA·h/g, with a capacity retention of 87.4% after 600 cycles at a current density of 1*C*. Furthermore, even at higher current densities of 5*C* and 10*C*, the LNMOZ20 electrode still demonstrates excellent stability with discharge capacities reaching 111.7 and 103.6 mA·h/g, and capacity retentions maintaining at 81.0% and 101.4% after 2000 cycles, respectively. This study highlights that the incorporation of an ultrathin ZrO_2 layer by ALD is an effective strategy for enhancing the long-term cycling stability of LNMO cathodes.

Key words: spinel $LiNi_{0.5}Mn_{1.5}O_4$; ZrO_2 coating; high-voltage cathode; atomic layer deposition; cathode electrolyte interphase film

1 Introduction

Transition metal (TM) oxides present a promising choice for next-generation electrode materials of lithium-ion batteries (LIBs) due to their high specific capacity and cost-effectiveness. The typical TM oxides cathode materials include $LiCoO_2$, $LiNi_xCo_yAl_{1-x-y}O_2$ (NCA) and $LiNi_xMn_yCo_{1-x-y}O_2$ (NMC) [1−3]. However, the rising cost of cobalt poses economic challenges [4−6]. Considering cost implications, cobalt (Co)-free cathodes have emerged as promising candidates. Among the Co-free cathodes, the spinel $LiNi_{0.5}Mn_{1.5}O_4$ (LNMO) distinguishes itself by a high voltage plateau (≈4.7 V (vs Li^+/Li)) and a 3D lithium-ion diffusion channel [7]. The high operating voltage of LNMO arising from the Ni^{2+}/Ni^{4+} redox couple and its specific capacity of 147 mA·h/g confer a high theoretical energy density of 650 W·h/kg which is comparable to that of NMC [8]. The absence of cobalt in LNMO, as compared to NMC, further enhances the advantage of LNMO as a cathode. Despite its promising attributes, LNMO cathode encounters challenges that include irreversible surface phase transition, transition metal dissolution, Jahn−Teller distortion of Mn^{3+} and electrolyte oxidation [9−12].

Researchers have employed various strategies to address these issues, such as formulating new

Corresponding author: Yuan-zhi CHEN, Tel: +86-592-2181637, E-mail: yuanzhi@xmu.edu.cn;
Dong-liang PENG, Tel: +86-592-2180155, E-mail: dlpeng@xmu.edu.cn
https://doi.org/10.1016/S1003-6326(25)66939-1

electrolyte compositions, implementing surface modifications on the electrode through organic and inorganic coatings, customizing the binders, altering synthetic conditions to adjust cation (Mn and Ni) ordering, doping cations, and adjusting particle size and morphology. Among these strategies, inorganic surface coatings, such as Al_2O_3 [13], Fe_2O_3 [14], RuO_2 [15], Li_3PO_4 [16], and Li_2ZrO_3 [17], have been coated on the LNMO surface to establish a stable electrode−electrolyte interface and minimize the direct contact area between electrolyte and electrode.

Atomic layer deposition (ALD), an advanced vapor deposition technique capable of creating ultrathin and uniform layers with precise control over thickness [18,19], has recently been applied to the synthesis of LIB materials to form a homogeneous coating layer and ameliorating interfacial problems. ALD ensures that only one layer of atoms is deposited in each reaction cycle, contributing to the precise and controlled growth of thin films with atomic-scale accuracy [20−23]. The ultrathin coating layer deposited by ALD does not block the original electrical path, but facilitates Li^+ diffusion instead. Recently, ALD technology has been applied to cathodes, anodes, electrolytes and separators for improving the electrochemical performance of LIBs [24]. Deposition materials such as MgO [25], TiO_2 [26], and ZrO_2 [18,19,27] are usually employed. Among the coating materials, ZrO_2 is especially attractive due to its high dielectric constant and enhanced electrochemical property. As an available HF scavenger, ZrO_2 coating layers can suppress the Mn dissolution and reduce the contact area between cathode and electrolyte [28−30]. Moreover, appropriate ZrO_2 with high chemical stability can enhance the thermal stability of cathode material, thereby reducing the volume expansion and structural damage during charge and discharge. ZrO_2 protective layer was shown to play a crucial role in mitigating degradation and promoting overall stability and longevity in the performance of LIBs [31−34].

Herein, ALD technology was employed to deposit an ultrathin ZrO_2 coating layer on the surfaces of LNMO particles synthesized by a hydrothermal method, aiming to reduce side reaction between LNMO cathode and electrolyte, and enhance the long-term cycling stability of LNMO. It was found that the ultrathin ZrO_2 coating layer with appropriate thickness may serve to protect the LNMO surface structure during charge and discharge, improve the structure stability, alleviate the interface reaction between the electrolyte and the cathode material, thereby achieving long-term cycling stability.

2 Experimental

2.1 Synthesis of LNMO

The primary LNMO was synthesized through a hydrothermal method using chemically pure reagents without further refinement. The synthetic process was detailed as follows: 3 mmol $Mn(CH_3COO)_2{\cdot}4H_2O$, 1 mmol $Ni(CH_3COO)_2{\cdot}4H_2O$ and 1 g polyvinylpyrrolidine (PVP) were dissolved in 50 mL glycol and stirred to obtain a green transparent solution labeled as Solution A. Simultaneously, 20 mmol NH_4HCO_3 was dissolved in 10 mL deionized water and 16 mL polyethylene glycol (PEG 600) to obtain Solution B. Solution B was added to Solution A drop by drop with continuous stirring. After forming a uniform solution, the mixtures were transferred into a Teflon-lined hydrothermal reactor and reacted at 180 °C for 10 h, followed by natural cooling to room temperature. The resulting hydroxide was collected after washing with deionized water and ethanol, and subsequently dried at 80 °C. The hydroxide was subjected to presintering at 500 °C for 5 h and allowed to naturally cool to room temperature, obtaining the oxide precursor. Subsequently, the oxide precursor was milled with a stoichiometric amount of $LiOH{\cdot}H_2O$ and calcined at 800 °C for 12 h to obtain the final LNMO product.

2.2 Synthesis of LNMO with ultrathin ZrO_2 coating

The deposition of ZrO_2 on LNMO powders was performed in a Yunmao GM10 Powder ALD system using tetrakis(ethylmethylamino)zirconium (TEMAZ) and H_2O as raw materials. During one single deposition cycle, TEMAZ and H_2O were introduced alternatively into the process chamber. Argon was used as purging and carrier gas. The thickness of ZrO_2 layer was adjusted by varying the number of deposition cycles, and each of the sample was denoted as LNMOZ*n* (*n*=10, 20 and 40).

2.3 Material characterization

The crystal structure of the cathode materials was determined using a Bruker-axs X-ray diffractometer (XRD) with a Cu K_α radiation. The morphology was observed by scanning electron microscopy (SEM) using a Hitachi SU−70 instrument. Transmission electron microscopy (TEM) images were acquired with a Talos F200s transmission electron microscope. The X-ray photoelectron spectroscopy (XPS) was employed to ascertain the chemical valence states by utilizing a Thermo Scientific ESCALAB Xi+ spectrometer. Infrared spectroscopy analyses were performed using a Nicolet iS10 FTIR spectrometer manufactured by Thermo Fisher Scientific.

2.4 Electrochemical performance measurements

The electrodes were fabricated by blending 80 wt.% of active materials, 10 wt.% acetylene black, and 10 wt.% polyvinylidene fluoride (PVDF), which were homogenously mixed in N-methyl-2-pyrrolidone (NMP). The prepared slurry was coated onto carbon-coated aluminum foil and subsequently dried at 80 °C in a vacuum oven. The CR2025-type coin half-cells were assembled within an argon-filled glove box, while the separator was Celgard 2325 membrane, the counter electrode was Li metal foil, and the electrolyte was a mixture of fluoro-ethylene carbonate (FEC), 1, 1, 2, 2-tetrafluoroethy-2′, 2′, 2′-trifluoroethyl ether (HFE), and 3, 3, 3-fluoroethylmethyl carbonate (FEMC) in a volume ratio of 2:2:6, and contained 1 mol/L $LiPF_6$ and 0.02 mol/L lithium difluoro(oxalato) borate (LiDFOB).

The galvanostatic charge−discharge tests at various current densities (1C=147 mA/g) were carried out via LAND testing system (Wuhan LAND Electronics Ltd.) and Neware testing system (Neware Technology Limited). The cyclic voltammetry (CV) curves at 3.5−4.95 V with 2 mV/s were evaluated through CHI660C electrochemical workstation. The electrochemical impedance spectroscopy (EIS) spectrum at frequency ranging from 100 kHz to 0.01 Hz was obtained by a Parstat 3000−DX electrochemical workstation.

3 Results and discussion

3.1 Chemical reaction during ALD process

Figure 1 shows the schematic diagram of depositing an ultrathin ZrO_2 layer on the LNMO surface via the ALD technique. The surface of LNMO is hydroxylated by prepulsed water vapor to begin the reaction before the metal source precursor TEMAZ enters into the reaction chamber. The hydroxyl groups then react with TEMAZ to form $Zr[N(C_2H_5)(CH)_3]_2$ monolayers connecting with LNMO through oxygen atoms derived from dehydrogenated hydroxyl groups [35]. Additional physically adsorbed layers and byproducts resulting from the reaction of one alkylamine molecule are removed by argon flow before introducing the second reactant. In the second half-reaction, water serves as the oxygen source and reacts with the $Zr[N(C_2H_5)(CH)_3]_2$ layer on the surface of LNMO, yielding the desired ZrO_2 and generating new reactive sites on the substrate. Redundants and byproducts are subsequently purged from the reactor via a pure argon flow. The sequence of alternating half-reactions is repeated iteratively, facilitating the formation of ultrathin ZrO_2 coating on surface of LNMO. This controlled layering process enables precise and uniform deposition of the ZrO_2 coating on the surface of LNMO.

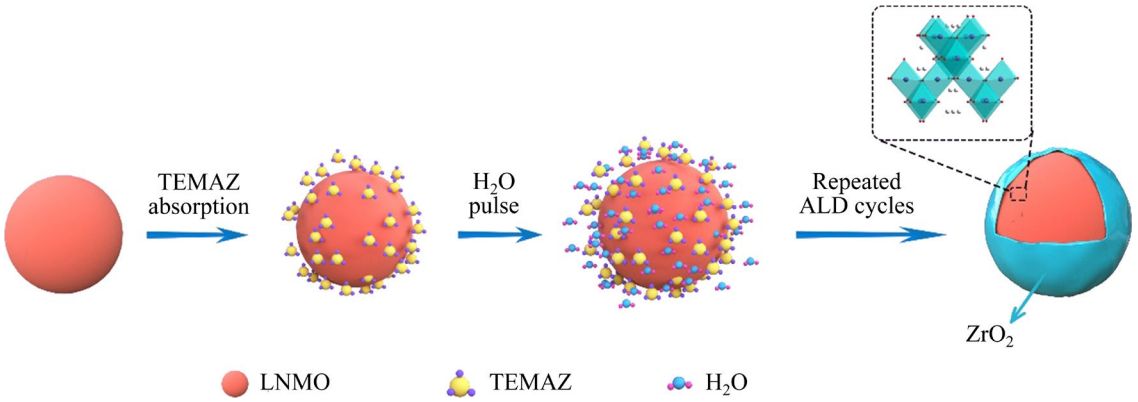

Fig. 1 Schematic diagram of production of LNMO with ultrathin ZrO_2 coating by ALD technology

3.2 Structure, composition and morphology

The XRD patterns in Fig. 2(a) present a comprehensive view of both LNMO and ZrO_2 modified LNMO samples. All diffraction peaks are in consistent with the standard card (PDF#80-2162) which corresponds to LNMO with $Fd\bar{3}m$ space group [36]. The XRD Rietveld refinements of LNMO, LNMOZ10, LNMOZ20 and LNMOZ40 are shown in Figs. S1(a−d) in Supplementary Information (SI), respectively, and the corresponding data are listed in Table S1 in SI. A noteworthy observation is the consistent decrease in the lattice parameter of the samples with an increasing amount of ZrO_2. This reduction is ascribed to the augmented microstrain during the incorporation of ZrO_2.

The structural disordering of the spinel LNMO can be distinguished by FTIR patterns shown in Fig. 2(b). A discernible reduction in the intensity Ni—O bond at 587 cm^{-1} in comparison to that of the Mn—O bond at 626 cm^{-1} is observed as the degree of disordering decreases [37]. The FTIR patterns consistently display similar intensities at 587 cm^{-1} for all four materials, signifying analogous disordering structures. Notably, the absence of characteristic peaks at 646, 464 and 430 cm^{-1} in the FTIR patterns Fig. S2 in SI) belonging to $P4_332$ phase implies that the four LNMO materials can be attributed to the $Fd\bar{3}m$ space group with disordered cations. This comprehensive analysis further enriches the understanding of the intricate interplay between ZrO_2 modification and the structure of LNMO materials.

XPS was applied to analyzing the chemical composition and state of the samples' surface. The XPS peaks ascribing to Mn $2p_{3/2}$ and Mn $2p_{1/2}$ can be clearly observed in the Mn 2p spectra (Fig. S1(e) in SI). These peaks can be further divided to discern the presence of Mn^{3+} and Mn^{4+}. The peaks at about 641.7 and 653.3 eV are ascribed to Mn^{3+}, while the peaks at about 642.9 and 654.2 eV are ascribed to Mn^{4+} [38,39]. The shift of Mn 2p characteristic peak towards lower binding energy indicates the decrease of Mn valence state. The Mn oxidation state can be distinguished using the Mn 3s peak, which displays two multiplet split components resulting from the coupling of non-ionized 3s electrons

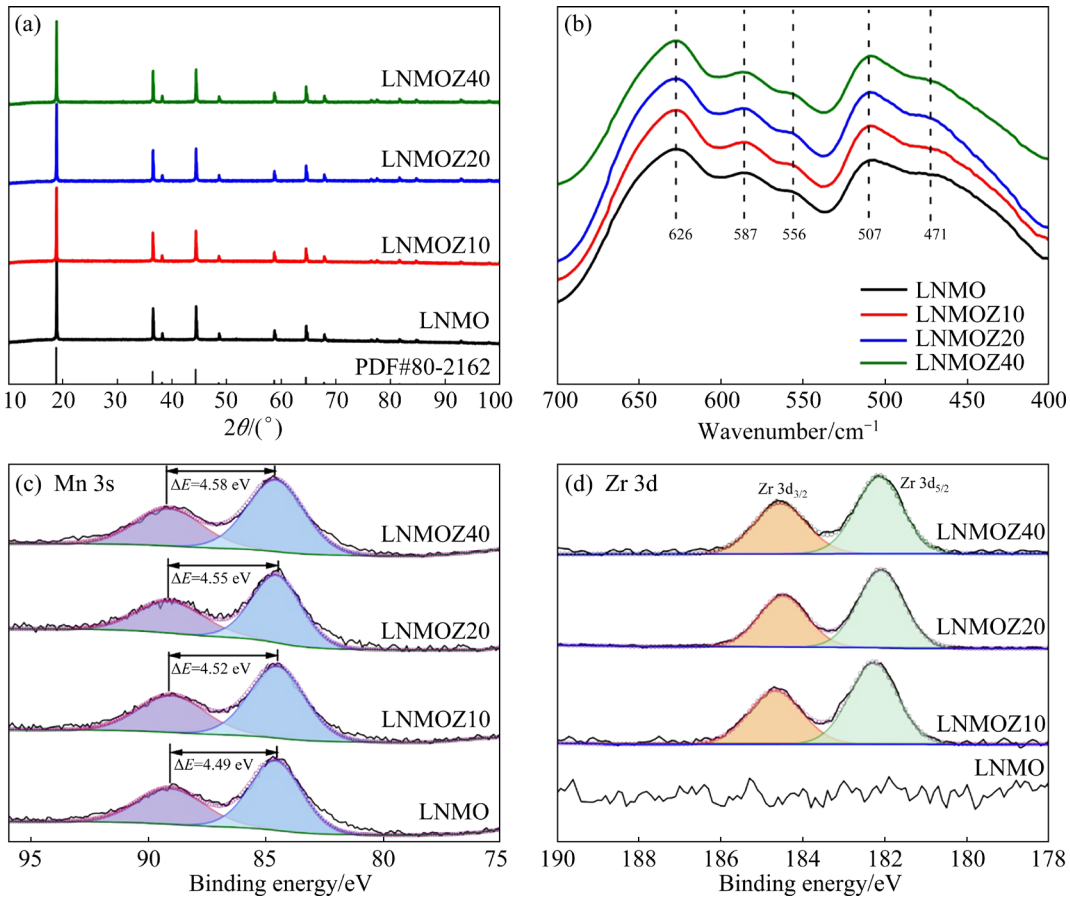

Fig. 2 XRD patterns (a), FTIR patterns (b), Mn 3s XPS spectra (c) and Zr 3d XPS spectra (d) of different samples

with 3d valence-band electrons, as shown in Fig. 2(c). The fact that the energy difference (ΔE) between the two splitting peaks is larger than 4.7 eV indicates that the valence state of Mn is less than +4. The increase of ΔE indicates a decrease in Mn valence with increasing the content of ZrO_2. The Mn valence (v_{Mn}) can be calculated via the following equation [40]:

$$v_{Mn}=9.67-1.27\Delta E_{3s}/\text{eV} \quad (1)$$

The calculated Mn valences of the LNMO, LNMOZ10, LNMOZ20, and LNMOZ40 samples are +3.96, +3.93, +3.89 and +3.85, respectively. The decrease of Mn valences can be attributed to the existence of the ZrO_2 layer that changes the chemical environment of the surface of LNMO particles [26]. This is related to the reducibility resulted from Lewis acidity of TEMAZ during the deposition. Increased deposited layers and treatment time with TEMAZ lead to the decrease of valence state.

The Zr 3d XPS spectra are shown in Fig. 2(d). It is obvious that Zr element is absent in the pristine LNMO material, while there are apparent Zr peaks in LNMOZ10, LNMOZ20 and LNMOZ40. LNMOZ40 exhibits a stronger characteristic peak due to the higher content of ZrO_2 in surface layer. The characteristic peaks at approximately 182.2 and 184.6 eV are ascribed to Zr $3d_{5/2}$ and Zr $3d_{3/2}$, respectively [41−43]. The Zr 3d XPS spectra with a difference value of 2.4 eV between the two split peaks indicate that the valence of Zr is almost +4 [44]. Additionally, the Ni 2p spectra in Fig. S1(f) in SI display no obvious binding energy shift, indicating no alteration in the valence of Ni.

The morphological details of the four samples were characterized by SEM. As shown in Figs. 3(a−d), the ZrO_2 modified LNMO particles have an average size of approximately 500 nm. There is no significant change in the morphology of LNMO after ZrO_2 modification, which indicates that the surface coating does not alter the morphology of the LNMO material. To gain a more detailed understanding of the sample's structure, TEM analyses were performed on LNMO (Figs. S3(a, b) in SI) and LNMOZ20 (Figs. 3(e−g)) samples. Both materials exhibit near-spherical particles with a diameter of around 500 nm, which is consistent with the observation results of SEM. The HRTEM images of LNMO (Figs. S3(a, b) in SI) reveal a well-crystallized structure with lattice fringes viewed in the [110] zone axis of a $Fd\bar{3}m$ cubic structure, which is very similar to the LNMO particles prepared by blow-spinning technique [45]. For LNMOZ20 sample, the deposition of ZrO_2 does not obviously change the crystalline structure of LNMO. As shown in Fig. 3(g), lattice fringes viewed in the [111] zone axis of a $Fd\bar{3}m$ cubic structure are clearly seen. In addition, an amorphous layer at the particle edge is also observed (Fig. 3(f)). EDS analyses (Figs. S3(c, d) in SI) in the edge layer confirm the presence of Zr and O, suggesting the covering of ZrO_2 layer. Along with the XPS results on the valence (+4) of Zr, the above characterizations strongly indicate that an ultrathin ZrO_2 layer has been deposited on the surface of LNMO particles, which bring significant impact to the electrochemical performances of LNMO cathodes.

3.3 Electrochemical performance

The electrochemical performance of LNMO and ZrO_2 modified LNMO was evaluated through CR2025 coin cell. CV measurements were applied to investigating the oxidation/reduction behavior of all samples, and the results are presented in Fig. 4(a). It is obvious that all samples exhibit a pair of split peaks at approximately 4.7 V, which can be ascribed to Ni^{2+}/Ni^{3+} and Ni^{3+}/Ni^{4+} redox couples. Additionally, a small peak at approximately 4.0 V corresponds to Mn^{3+}/Mn^{4+} redox couple [46]. The presence of the Mn^{3+}/Mn^{4+} redox couple suggests that all samples possess $Fd\bar{3}m$ structure with disordering cations, which agrees well with the findings from FTIR analysis. The observation that all four samples exhibit the same potential suggests a uniform and smooth penetration of Li-ions through the ZrO_2 coating layers. This uniformity in potential implies that the ZrO_2 modification does not hinder the effective transport of Li-ions during the charge−discharge cycles.

To explore the interfacial characteristics of the electrodes during cycling, the EIS measurements before and after cycling for 10 and 100 at 1C were carried out. Figure 4(b) illustrates the Nyquist plots obtained for all samples before cycling. The similarity observed in the EIS spectra among these four electrodes indicates a comparable reaction kinetic mechanism. Typically, EIS spectra consist of a semicircle in the high frequency range and an

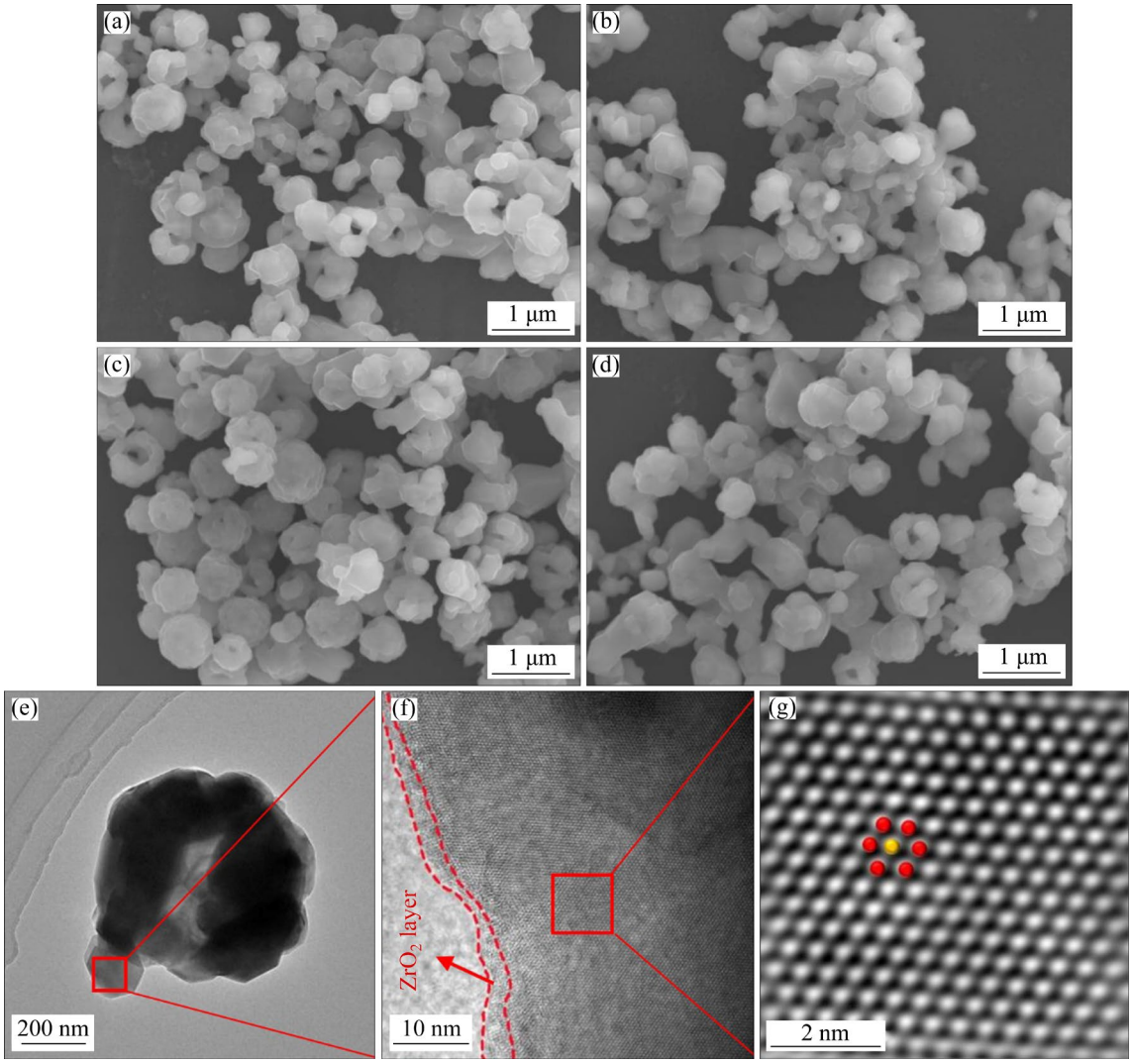

Fig. 3 SEM images of LNMO (a), LNMOZ10 (b), LNMOZ20 (c) and LNMOZ40 (d); TEM (e, f) and HRTEM (g) images of LNMOZ20

oblique line in the low frequency range. The intercept of these spectra represents ohmic resistance (R_s), and the semicircle in high frequency reflects to charge transfer impedance (R_{ct}) [47,48]. The detailed fitting EIS results before cycling are listed in Table S2 in SI. Notably, the R_{ct} values of four electrodes with LNMO, LNMOZ10, LNMOZ20 and LNMOZ40 are 490.7, 487.6, 268.2 and 203.5 Ω, respectively. It is obvious that the R_{ct} decreases with increasing ZrO_2 content since the deposited ZrO_2 layer facilitates ion transport [49]. The EIS spectra after cycling are shown in Figs. 4(c, d). The EIS spectra after cycling usually appear a second semicircle in the middle frequency region, indicating a resistance value of the cathode electrolyte interphase (CEI) generated during the cycling [48]. After 10 cycles, the ZrO_2 modified electrodes have smaller resistance of the CEI comparing to pristine LNMO, which indicates that the ultrathin ZrO_2 coating layer can effectively restrain the growth of CEI [49]. Meanwhile, after 100 cycles, it is obvious that the radius of the second semicircle of LNMOZ20 is the minimum, indicating the lowest resistance of Li^+ diffusion. Apparently, the results ascribe that the ultrathin ZrO_2 layer may effectively suppress the dissolution of the transition metal and reduce the contact area with electrolyte. A similar result was obtained for ZrO_2 coated $LiNi_{0.4}Co_{0.2}Mn_{0.4}O_2$ cathode, in which the ultrathin ZrO_2 coating layer is shown to effectively inhibit the charge transfer impedance and significantly promote the deintercalation of Li

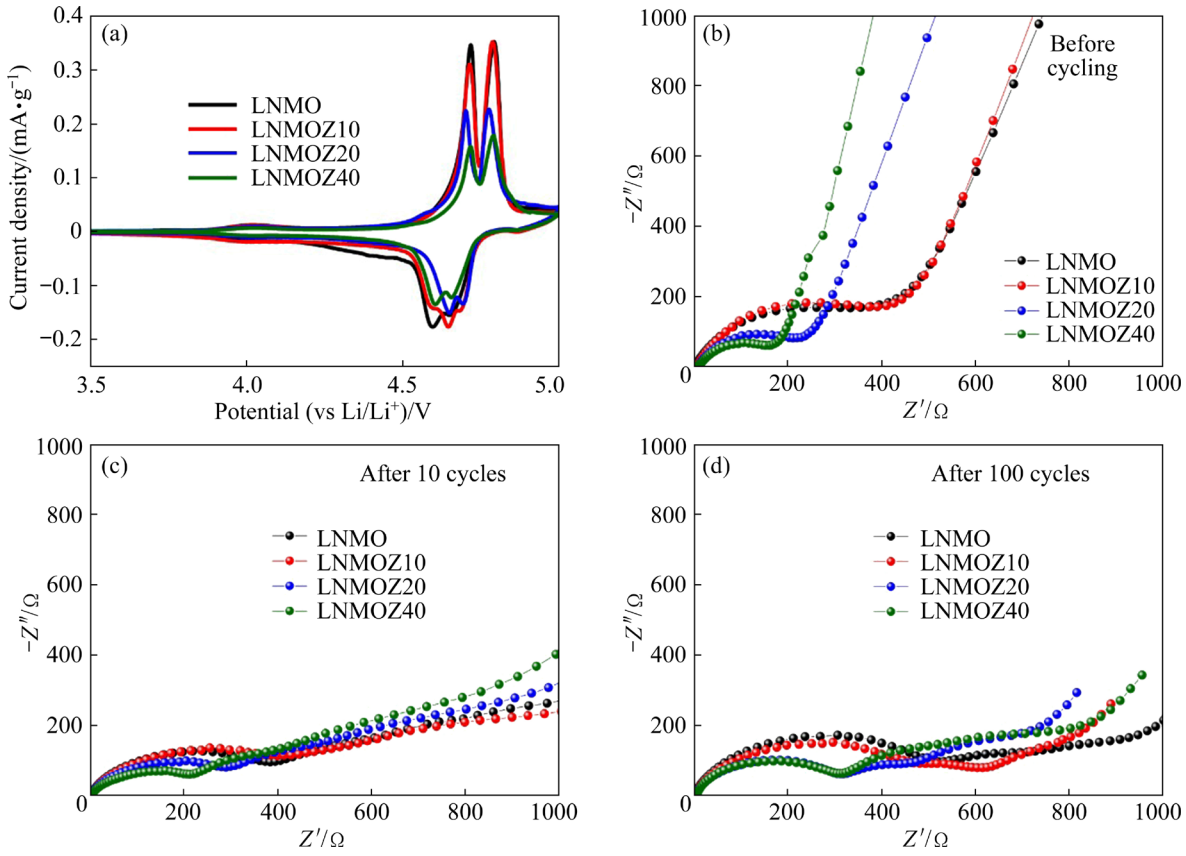

Fig. 4 CV curves (a) and Nyquist plots before cycling (b) and after 10 cycles (c) and 100 cycles (d) of different samples at 1*C*

ions and electron conduction [50].

The initial charge−discharge curves are shown in Fig. 5(a). All curves exhibit an obvious long voltage plateau at approximately 4.7 V which is ascribed to the Ni^{2+}/Ni^{4+} redox processes, while a short voltage plateau at approximately 4.0 V also appears, attributing to the Mn^{3+}/Mn^{4+} redox process [38]. The characteristics of charge−discharge curves are consistent with the CV curves, indicating the typical electrochemical behavior of LNMO cathode material. In addition, the discharge specific capacities at a current density of 0.1*C* are 133.8, 130.6, 131.3 and 114.9 mA·h/g, respectively, for LNMO, LNMOZ10, LNMOZ20 and LNMOZ40. The discharge specific capacity decreases with increasing the ZrO_2 content, indicating no capacity contribution of ZrO_2 to the electrochemical behavior. Figure 5(b) illustrates the rate performance of all samples at various current densities ranging from 0.1*C* to 10*C*. The enhanced rate performance clearly shows the advantages of the ultrathin ZrO_2 coating layer. It is evident that the discharge specific capacity of the modified electrode is less than that of pristine sample when the ZrO_2 content is the maximum (LNMOZ40). This is because ZrO_2 is not a battery material and lacks the ability to delocalize the embedded Li ions. Consequently, the specific capacity of the electrode decreases when the ZrO_2 content increases. For LNMOZ40, the capacity at 0.1*C* is lower than that at 0.3*C*, which may be attributed to the incomplete activation, and the increase of ZrO_2 thickness may lead to an increase of activation cycle number [46]. During cycling, the formation of CEI is inevitable. The ultrathin ZrO_2 coating layer can effectively restrain the continuous growth of CEI. The ultrathin CEI film can not only facilitate Li-ion transport and electron conduction, but also inhibit electrolyte corrosion. Meanwhile, the ultrathin ZrO_2 layer also reduces the polarization on the electrode surface with reduced over-potential [18]. It is obvious that the LNMOZ20 shows the best electrochemical performance, which indicates a suitable deposition thickness.

To assess the long-term stability of the LNMO materials, extended cycle tests were conducted.

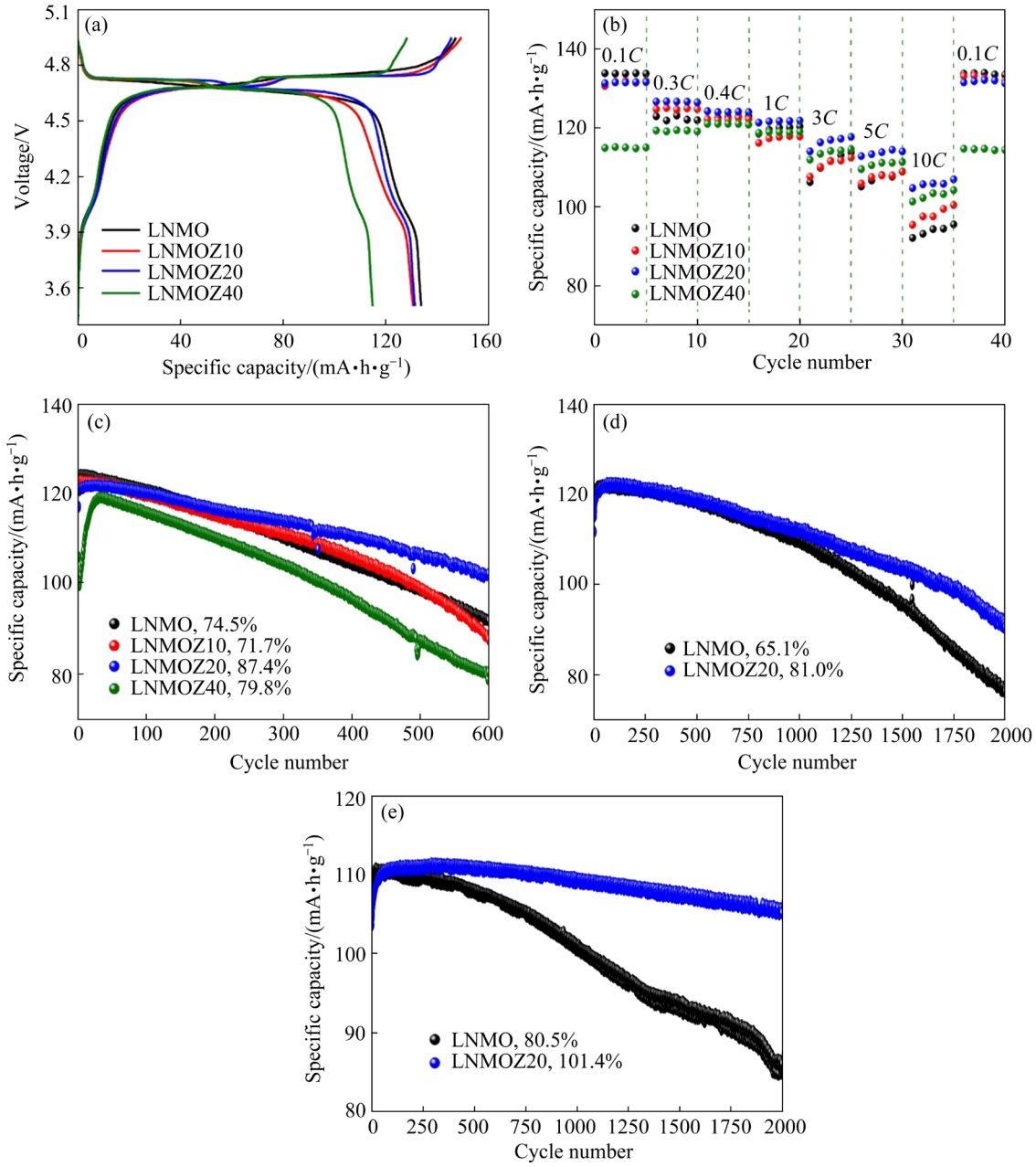

Fig. 5 (a) Initial charge−discharge curves at 0.1*C* of different samples; (b) Rate performances of different samples; (c, d, e) Long cycling performances of different samples at 1*C*, 5*C* and 10*C*, respectively

Figure 5(c) shows the electrochemical performance of all electrodes at 1*C*. The initial discharge specific capacities are 123.0, 122.3, 117.1 and 99.7 mA·h/g, respectively, for LNMO, LNMOZ10, LNMOZ20 and LNMOZ40. The discharge specific capacity of pristine LNMO fades to 91.9 mA·h/g after 600 cycles, while that of LNMOZ20 still keeps a value of 102.3 mA·h/g. The capacity retentions of all electrodes are 74.5%, 71.7%, 87.4% and 79.8%, respectively, for LNMO, LNMOZ10, LNMOZ20 and LNMOZ40. The LNMOZ20 exhibits the best electrochemical performance. It can be found that when ZrO_2 is deposited, a capacity increase stage appears in a certain degree, which is a result of the activation phenomenon caused by the ultrathin ZrO_2 layer.

LNMO and LNMOZ20 were selected for further tests at high current densities. The galvanostatic charge−discharge tests of LNMO and LNMOZ20 at 5*C* and 10*C* were conducted. As shown in Figs. 5(d, e), the initial discharge specific capacities of LNMO are 117.2 and 106.8 mA·h/g at

5*C* and 10*C*, respectively, while those of LNMOZ20 are 111.7 and 103.6 mA·h/g at 5*C* and 10*C*, respectively. LNMO remains 65.1% and 80.5% of its initial discharge specific capacity after 2000 cycles at 5*C* and 10*C*, respectively. Meanwhile, the LNMOZ20 has 81.0% of its discharge specific capacity left at 5*C* and 101.4% at 10*C* in comparison to the initial discharge capacity. A comparison to other published literatures on surface coated-LNMO is listed in Table S3 is SI.

The discharge capacities of LNMOZ20 at 5*C* and 10*C* also increase at the initial stage of cycling (Figs. 5(d, e)), which should be due to the activation phenomenon caused by the ultrathin ZrO_2 layer, and the activation cycle number increases with the increase of ZrO_2 layer thickness. The ultrathin ZrO_2 layer ensures the chemical stability of LNMO cathode, resulting in an excellent cycling stability for LNMO. Particularly, the LNMOZ20 delivers the highest capacity retention at 1*C*, 5*C* and 10*C* after a long-term cycling. These results obtained demonstrate a noteworthy enhancement in capacity and extended cycle life for LNMO when modified with ultrathin ZrO_2 coating layer produced by ALD using 20 deposition layers.

3.4 Characteristics after cycling

To further evaluate the contribution of the ultrathin ZrO_2 coating layer to improving the electrochemical performance of LNMO, the LNMO and LNMOZ20 electrodes after 600 cycles were analyzed via TEM and XPS. As shown in Fig. 6, the particles of pristine LNMO form cracks after 600 cycles, and an amorphous CEI film appears on the surface. In addition, there are many defects in the lattices, which may be caused by the transition metal rearrangement, indicating a structural collapse of LNMO [51]. In contrast, LNMOZ20 particles are relatively complete with much less lattice defects, indicating that the structural integrity of LNMOZ20 is well maintained.

XPS was used to analyze the difference of CEI components on the surface of LNMO and LNMOZ20 after 600 cycles. As shown in Fig. 7, the

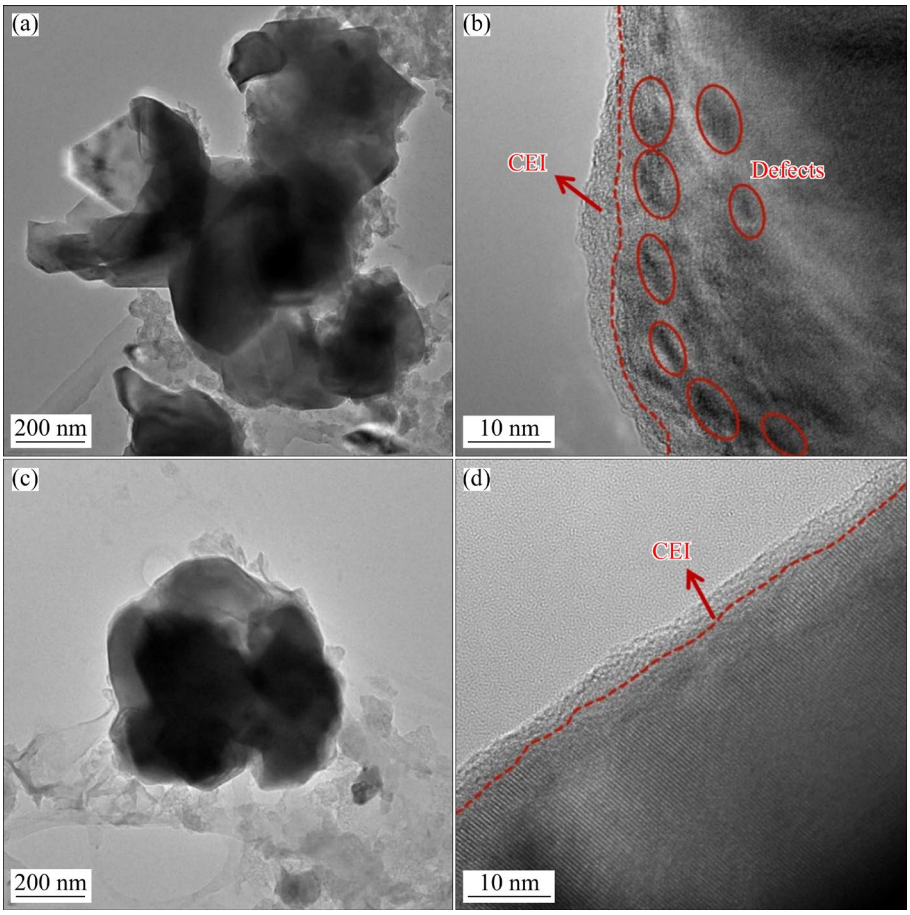

Fig. 6 Low-magnification (a, c) and high-magnification (b, d) TEM images of LNMO (a, b) and LNMOZ20 (c, d) after 600 cycles

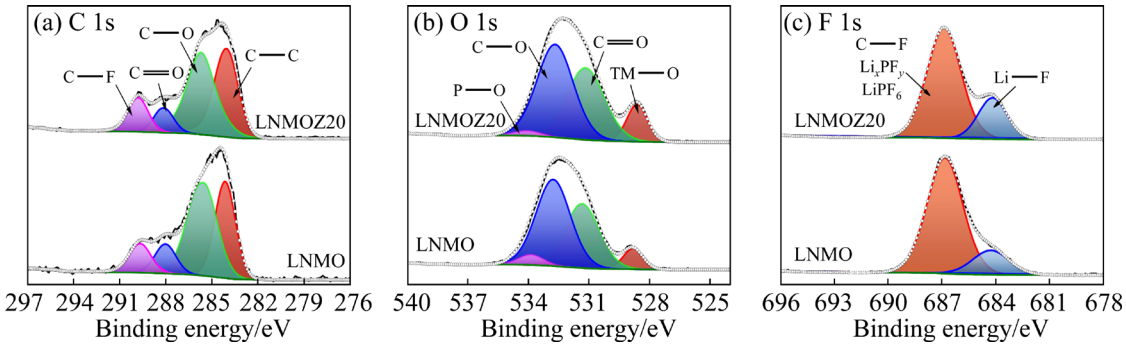

Fig. 7 C 1s (a), O 1s (b), and F 1s (c) spectra of LNMO and LNMOZ20 after 600 cycles

C 1s spectra (Fig. 7(a)) reveal C—C, C—O, C═O and C—F peaks attributing to the organics and carbonate groups in the CEI layer [13]. The C═O peak at around 288 eV is attributed to $LiCO_3$, which is a side product related to the oxidative decomposition of electrolyte. The C═O peak intensity in LNMOZ20 is weaker than that in LNMO, indicating that the CEI film formed in LNMOZ20 after cycling is thinner than that in LNMO. The O 1s spectra in Fig. 7(b) exhibit characteristic peaks of C—O, C═O, TM—O and P—O [40,52]. The peak intensity of TM—O in LNMOZ20 is stronger than that in LNMO, and peak intensity of P—O in LNMOZ20 is lower than that in LNMO, indicating less dissolution of TM in the LNMOZ20 after cycling. For F 1s spectra (Fig. 7(c)), there exist characteristic peaks of C—F and Li—F. The C—F peak with strong intensity is ascribed to the PVDF. The weaker peak at around 684 eV in LNMO indicates that less LiF is generated in LNMO than that in LNMOZ20. This means that more HF is generated in LNMO during the cycling, which increases the corrosion to the electrode material [51]. The above results of TEM and XPS indicate that the ultrathin ZrO_2 layer can effectively inhibit the corrosion of electrolyte and the dissolution of transition metal.

4 Conclusions

(1) Spinel LNMO cathode materials were synthesized and coated with ultrathin ZrO_2 surface layers by using the ALD technique. The thickness of the ZrO_2 coating layer can be conveniently adjusted by varying the number of deposition cycles. The electrochemical performance of LNMO is significantly affected by the ultrathin ZrO_2 surface layer.

(2) The LNMOZ20 cathode material exhibits a surprising capacity retention of 87.4% with a high capacity of 117.1 mA·h/g after 600 cycles at 1*C*, 81.0% capacity retention after 2000 cycles at 5*C*, and 101.4% capacity retention after 2000 cycles at 10*C*.

(3) The TEM and XPS characterization results after cycling show that the LNMOZ20 sample generates more uniform and stable CEI films which are conducive to the improvement of long-term cycle stability.

(4) The ultrathin ZrO_2 surface layer with appropriate thickness may effectively reduce the contact area between LNMO and the electrolyte, minimize the side reactions, promote the diffusion of Li ions, thereby enhancing the long-term cycling stability of LNMO cathode.

CRediT authorship contribution statement

Jie MEI: Methodology, Investigation, Formal analysis, Writing – Origin draft; **Qi-xiang XU:** Methodology; **Yuan-zhi CHEN:** Supervision, Conceptualization, Writing – Review & editing; **Gui-yang GAO:** Formal analysis; **Wan-jie XU:** Formal analysis; **Qing-shui XIE:** Formal analysis; **Lai-sen WANG:** Project administration; **Dong-liang PENG:** Supervision, Funding acquisition.

Declaration of competing interest

The authors declare that they have no known competing financial interests or personal relationships that could have appeared to influence the work reported in this paper.

Acknowledgments

This work was partially supported by the National Natural Science Foundation of China (Nos. 51931006, U22A20118).

Supplementary Information

Supplementary Information in this paper can be found at: https://tnmsc.csu.edu.cn/download/16-p4217-2024-0417-Supplementary_Information.pdf.

References

[1] MA Jun, HU Pu, CUI Guang-lei, CHEN Li-quan. Surface and interface issues in spinel $LiNi_{0.5}Mn_{1.5}O_4$: Insights into a potential cathode material for high energy density lithium ion batteries [J]. Chemistry of Materials, 2016, 28: 3578−3606.

[2] LIAN Meng-chen, SUN Qiang-chao, NIE Wei, LIU Yan-bo, DUAN Tong, CHENG Hong-wei, LU Xiong-gang. Na^+-doped layered $LiNi_{1/3}Co_{1/3}Mn_{1/3}O_2$ cathode derived from low nickel matte with high structural stability and fast diffusion kinetics [J]. Transactions of Nonferrous Metals Society of China, 2023, 33: 3100−3112.

[3] CAO Yuan-lin, YANG Xiu-kang, WANG Lu, XIAO Ling, FU Ni, ZOU Li, MA Wen-bo, LIU Zhe-ting, WANG Xiao-qin, LIU Li, SHU Hong-bo, WANG Xian-you. Improving electrochemical performance of Ni-rich layered oxide cathodes via one-step dual modification strategy [J]. Transactions of Nonferrous Metals Society of China, 2022, 32: 3663−3678.

[4] AISHOVA A, PARK G T, YOON C S, SUN Y K. Cobalt-free high-capacity Ni-rich layered $Li[Ni_{0.9}Mn_{0.1}]O_2$ cathode [J]. Advanced Energy Materials, 2020, 10: 1903179.

[5] GOONETILLEKE D, SHARMA N, PANG W K, PETERSON V K, PETIBON R, LI J, DAHN J R. Structural evolution and high-voltage structural stability of $Li(Ni_xMn_yCo_z)O_2$ electrodes [J]. Chemistry of Materials, 2019, 31: 376−386.

[6] LIANG G M, PETERSON V K, SEE K W, GUO Z P, PANG W K. Developing high-voltage spinel $LiNi_{0.5}Mn_{1.5}O_4$ cathodes for high-energy-density lithium-ion batteries: Current achievements and future prospects [J]. Journal of Materials Chemistry A, 2020, 8: 15373−15398.

[7] LIU Jing-jun, YUAN Ming-liang, LI Zhen, WANG Liang-hua, YAN Jun-qing, PENG Jing, OU Sheng-wen, XU Jing-yue. Influence of different raw materials on the preparation of single-crystal $LiNi_{0.5}Mn_{1.5}O_4$ by sol−gel method [J]. Journal of Alloys and Compounds, 2024, 971: 172778.

[8] BÖRNER M, NIEHOFF P, VORTMANN B, NOWAK S, WINTER M, SCHAPPACHER F M. Comparison of different synthesis methods for $LiNi_{0.5}Mn_{1.5}O_4$: Influence on battery cycling performance, degradation, and aging [J]. Energy Technology, 2016, 4: 1631−1640.

[9] LIANG Ge-meng, DIDIER C, GUO Zai-ping, PANG Wei-kong, PETERSON V K. Understanding rechargeable battery function using in operando neutron powder diffraction [J]. Advanced Materials, 2020, 32: e1904528.

[10] FANG Zhao, ZHANG Xing-liang, HOU Xue-yang, HUANG Wen-long, LI Lin-bo. Submicron single-crystalline $LiNi_{0.5}Mn_{1.5}O_4$ cathode with modulated Mn^{3+} content enabling high capacity and fast lithium-ion kinetics [J]. Rare Metals, 2022, 41: 2268−2279.

[11] XIAO Jie, CHEN Xi-lin, SUSHKO P V, SUSHKO M L, KOVARIK L, FENG Ji-jun, DENG Zhi-qun, ZHENG Jian-ming, GRAFF G L, NIE Zi-min, CHOI D, LIU Jun, ZHANG Ji-guang, WHITTINGHAM M S. High-performance $LiNi_{0.5}Mn_{1.5}O_4$ spinel controlled by Mn^{3+} concentration and site disorder [J]. Advanced Materials, 2012, 24: 2109−2116.

[12] LIU Hai-ping, LIANG Ge-meng, GAO Chao, BI Si-fu, CHEN Qiang, XIE Ying, FAN Shan-shan, CAO Li-xin, PANG Wei-kong, GUO Zai-ping. Insight into the improved cycling stability of sphere-nanorod-like micro-nano-structured high voltage spinel cathode for lithium-ion batteries [J]. Nano Energy, 2019, 66: 104100.

[13] LI Wei-kang, CHENG Di-yi, SHIMIZU R, LI Yi-xuan, YAO Wei-liang, RAGHAVENDRAN G, ZHANG Ming-hao, MENG Y S. Artificial cathode electrolyte interphase for improving high voltage cycling stability of thick electrode with Co-free 5 V spinel oxides [J]. Energy Storage Materials, 2022, 49: 77−84.

[14] WANG Gang, WEN Wei-cheng, CHEN Shu-hua, YU Rui-zhi, WANG Xian-you, YANG Xiu-kang. Improving the electrochemical performances of spherical $LiNi_{0.5}Mn_{1.5}O_4$ by Fe_2O_3 surface coating for lithium-ion batteries [J]. Electrochimica Acta, 2016, 212: 791−799.

[15] HONG Da, GUO Yu-feng, WANG Hui-xin, ZHOU Ji-gang, FANG Hai-Tao. Mechanism for improving the cycle performance of $LiNi_{0.5}Mn_{1.5}O_4$ by RuO_2 surface modification and increasing discharge cut-off potentials [J]. Journal of Materials Chemistry A, 2015, 3: 15457–15465.

[16] KONISHI H, SUZUKI K, TAMINATO S, KIM K, ZHENG Yue-ming, KIM S, LIM J, HIRAYAMA M, SON J Y, CUI Yi-tao, KANNO R. Effect of surface Li_3PO_4 coating on $LiNi_{0.5}Mn_{1.5}O_4$ epitaxial thin film electrodes synthesized by pulsed laser deposition [J]. Journal of Power Sources, 2014, 269: 293−298.

[17] ZHAO R, LI L, LI Y P, XU T H, PAN D, YU C Y, ZHAO H L, BAI Y. Decoration by dual-phase Li_2ZrO_3 islands with core–shell structures enhances the electrochemical performance of high-voltage $LiNi_{0.5}Mn_{1.5}O_4$ [J]. Applied Physics Letters, 2020, 116: 021601.

[18] AHN J, JANG E K, YOON S, LEE S J, SUN S J, KIM D H, CHO K Y. Ultrathin ZrO_2 on $LiNi_{0.5}Mn_{0.3}Co_{0.2}O_2$ electrode surface via atomic layer deposition for high-voltage operation in lithium-ion batteries [J]. Applied Surface Science, 2019, 484: 701−709.

[19] BAO Wen-da, QIAN Guan-nan, ZHAO Lian-qi, YU Yi, SU Long-xing, CAI Xin-can, ZHAO Hao-jie, ZUO Yu-qing, ZHANG Yue, LI Hao-yuan, PENG Zi-jian, LI Lin-sen, XIE Jin. Simultaneous enhancement of interfacial stability and kinetics of single-crystal $LiNi_{0.6}Mn_{0.2}Co_{0.2}O_2$ through optimized surface coating and doping [J]. Nano Letters, 2020, 20: 8832−8840.

[20] GEORGE S M. Atomic layer deposition: an overview [J]. Chemical Reviews, 2010, 110: 111−131.

[21] MA Lu, NUWAYHID R B, WU Tian-pin, LEI Yu, AMINE K, LU Jun. Atomic layer deposition for lithium-based batteries [J]. Advanced Materials Interfaces, 2016, 3: 1600564.

[22] MARICHY C, BECHELANY M, PINNA N. Atomic layer deposition of nanostructured materials for energy and

environmental applications [J]. Advanced Materials, 2012, 24: 1017−1032.

[23] MENG Xiang-bo, YANG Xiao-qing, SUN Xue-liang. Emerging applications of atomic layer deposition for lithium-ion battery studies [J]. Advanced Materials, 2012, 24: 3589−3615.

[24] AHMED B, XIA Chuan, ALSHAREEF H N. Electrode surface engineering by atomic layer deposition: A promising pathway toward better energy storage [J]. Nano Today, 2016, 11: 250−271.

[25] LASKAR M R, JACKSON D H, XU Shen-zhen, HAMERS R J, MORGAN D, KUECH T F. Atomic layer deposited MgO: A lower overpotential coating for $Li[Ni_{0.5}Mn_{0.3}Co_{0.2}]O_2$ cathode [J]. ACS Applied Materials & Interfaces, 2017, 9: 11231−11239.

[26] ZHANG Cong-cong, SU Jun-ming, WANG Tao, YUAN Kai-ping, CHEN Chun-guang, LIU Si-yang, HUANG Tao, WU Jian-hua, LU Hong-liang, YU Ai-shui. Significant improvement on electrochemical performance of $LiMn_2O_4$ at elevated temperature by atomic layer deposition of TiO_2 nanocoating [J]. ACS Sustainable Chemistry & Engineering, 2018, 6: 7890−7901.

[27] ZHAO Jian-qing, WANG Ying. Atomic layer deposition of epitaxial ZrO_2 coating on $LiMn_2O_4$ nanoparticles for high-rate lithium ion batteries at elevated temperature [J]. Nano Energy, 2013, 2: 882−889.

[28] JO S J, HWANG D Y, LEE S H. Use of zirconium dual-modification on the $LiNi_{0.8}Co_{0.1}Mn_{0.1}O_2$ cathode for improved electrochemical performances of lithium-ion batteries [J]. ACS Applied Energy Materials, 2021, 4: 3693−3700.

[29] ZHAO Jian-qing, QU Guo-ying, FLAKE J C, WANG Ying. Low temperature preparation of crystalline ZrO_2 coatings for improved elevated-temperature performances of Li-ion battery cathodes [J]. Chemical Communications, 2012, 48: 8108−8110.

[30] KAUR G, NESVADERANI F, HADIDI L, DUNN D, CAMPBELL S, GATES B D. Unraveling the role of composite Li_3PO_4/ZrO_2 coatings prepared by dry milling on high voltage spinel cathodes for lithium-ion batteries: Insights into lattice strain, thermal behavior, material compatibility, and electrochemical performance [J]. ACS Applied Energy Materials, 2022, 5: 14335−14352.

[31] LI D C, KATO Y, KOBAYAKAWA K, NOGUCHI H, SATO Y. Preparation and electrochemical characteristics of $LiNi_{1/3}Mn_{1/3}Co_{1/3}O_2$ coated with metal oxides coating [J]. Journal of Power Sources, 2006, 160: 1342−1348.

[32] LI Xi-fei, LIU Jian, MENG Xiang-bo, TANG Yong-ji, BANIS M N, YANG Jin-li, HU Yu-hai, LI Ru-ying, CAI Mei, SUN Xue-liang. Significant impact on cathode performance of lithium-ion batteries by precisely controlled metal oxide nanocoatings via atomic layer deposition [J]. Journal of Power Sources, 2014, 247: 57−69.

[33] WU H M, BELHAROUAK I, ABOUIMRANE A, SUN Y K, AMINE K. Surface modification of $LiNi_{0.5}Mn_{1.5}O_4$ by ZrP_2O_7 and ZrO_2 for lithium-ion batteries [J]. Journal of Power Sources, 2010, 195: 2909−2913.

[34] ZHAO Jian-qing, AZIZ S, WANG Ying. Hierarchical functional layers on high-capacity lithium-excess cathodes for superior lithium ion batteries [J]. Journal of Power Sources, 2014, 247: 95−104.

[35] KANOMATA K, TOKORO K, IMAI T, PANSILA P, MIURA M, AHMMAD B, KUBOTA S, HIRAHARA K, HIROSE F. Room-temperature atomic layer deposition of ZrO_2 using tetrakis(ethylmethylamino)zirconium and plasma-excited humidified argon [J]. Applied Surface Science, 2016, 387: 497−502.

[36] KIM J H, MYUNG S T, YOON C S, KANG S G, SUN Y K. Comparative study of $LiNi_{0.5}Mn_{1.5}O_{4-\delta}$ and $LiNi_{0.5}Mn_{1.5}O_4$ cathodes having two crystallographic structures: $Fd\bar{3}m$ and $P4_332$ [J]. Chemistry of Materials, 2004, 16: 906−914.

[37] KUNDURACI M, AMATUCCI G G. Synthesis and characterization of nanostructured 4.7 V $Li_xMn_{1.5}Ni_{0.5}O_4$ spinels for high-power lithium-ion batteries [J]. Journal of the Electrochemical Society, 2006, 153: A1345−A1352.

[38] LI Li, ZHAO Rui, PAN Du, YI Shu-hong, GAO Liu-fei, HE Guan-jie, ZHAO Hui-ling, YU Cai-yan, BAI Ying. Constructing tri-functional modification for spinel $LiNi_{0.5}Mn_{1.5}O_4$ via fast ion conductor [J]. Journal of Power Sources, 2020, 450: 227677.

[39] ZHANG Jian-ning, SUN Gang, HAN Yi, YU Fu-da, QIN Xiu-juan, SHAO Guang-jie, WANG Zhen-bo. Boosted electrochemical performance of $LiNi_{0.5}Mn_{1.5}O_4$ via synergistic modification of Li^+-conductive Li_2ZrO_3 coating layer and superficial Zr-doping [J]. Electrochimica Acta, 2020, 343: 136105.

[40] YAN Chen-hui, SHAO Qi-nong, YAO Zhi-hao, GAO Ming-xi, ZHANG Chen-yang, CHEN Gai-rong, SUN Qian-wen, SUN Wen-ping, LIU Yong-feng, GAO Ming-xia, PAN Hong-ge. Multifunctional surface construction for long-term cycling stability of Li-rich Mn-based layered oxide cathode for Li-ion batteries [J]. Small, 2022, 18: e2107910.

[41] BETHGE O, HENKEL C, ABERMANN S, POZZOVIVO G, STOEGER-POLLACH M, WERNER W S M, SMOLINER J, BERTAGNOLLI E. Stability of La_2O_3 and GeO_2 passivated Ge surfaces during ALD of ZrO_2 high-k dielectric [J]. Applied Surface Science, 2012, 258: 3444−3449.

[42] HUANG You-yuan, CHEN Ji-tao, NI Jiang-feng, ZHOU Heng-hui, ZHANG Xin-xiang. A modified ZrO_2-coating process to improve electrochemical performance of $Li(Ni_{1/3}Co_{1/3}Mn_{1/3})O_2$ [J]. Journal of Power Sources, 2009, 188: 538−545.

[43] OH N K, KIM J T, KANG G, AN J K, NAM M, KIM S Y, PARK I S, YUN J Y. Oxidant effect of $La(NO_3)_3\cdot 6H_2O$ solution on the crystalline characteristics of nanocrystalline ZrO_2 films grown by atomic layer deposition [J]. Applied Surface Science, 2017, 394: 231−239.

[44] CUI Jian-dong, WU Hua-ting, ZHANG Yan, XU Yao-hua, YANG Zhi-min. Structure and properties of ZrCoCe getter film with Pd protection layer [J]. Rare Metals, 2021, 40: 2579−2583.

[45] TIAN Te, LU Lei-lei, YIN Yi-chen, TAN Yi-hong, ZHANG Tian-wen, LI Feng, YAO Hong-bin. Trace doping of multiple elements enables stable cycling of high areal capacity $LiNi_{0.5}Mn_{1.5}O_4$ cathode [J]. Small, 2022, 18: e2106898.

[46] ZONG Bo, DENG Zi-yao, YAN Shu-hao, LANG Ya-qiang, GONG Jia-jia, GUO Jian-ling, WANG Li, LIANG Guang-

chuan. Effects of Si doping on structural and electrochemical performance of $LiNi_{0.5}Mn_{1.5}O_4$ cathode materials for lithium-ion batteries [J]. Powder Technology, 2020, 364: 725−737.

[47] HUANG Yu-zhu, XING Lin, PEI Shuang, ZHOU Wei, HU Yu-jie, DENG Wei-na, CHEN Liang, ZHU Hai, CHEN Han. Co_9S_8/CNTs microspheres as superior-performance cathodes in aqueous ammonium-ion batteries [J]. Transactions of Nonferrous Metals Society of China, 2023, 33: 3452−3464.

[48] LI Yun-chao, WAN Shun, VEITH G M, UNOCIC R R, PARANTHAMAN M P, DAI Sheng, SUN Xiao-guang. A novel electrolyte salt additive for lithium-ion batteries with voltages greater than 4.7 V [J]. Advanced Energy Materials, 2017, 7: 1601397.

[49] ZHANG Wen, CHENG Fang-yuan, CHANG Miao, XU Yue, LI Yu-yu, SUN Shi-xiong, WANG Liang, XU Lei-min, LI Qing, FANG Chun, WANG Meng, LU Yu-hao, HAN Jian-tao, HUANG Yun-hui. Surface-interspersed nanoparticles induced cathode−electrolyte interphase enabling stable cycling of high-voltage $LiCoO_2$ [J]. Nano Energy, 2024, 119: 109031.

[50] LIU Jing-jun, YUAN Ming-liang, XIE Tang-feng, YAN Guan-jie. Ultrathin-ZrO_2-coated $LiNi_{0.4}Co_{0.2}Mn_{0.4}O_2$ cathode material for Li-ion batteries: Synthesis and electrochemical performance [J]. Journal of Materials Research, 2022, 37: 1019−1029.

[51] LU Di, CHEN Yu-feng, SUN Wei-wei, XIE Wie, YI Shuai-yu, LUO Shi-qiang, ZUO Lan-lan, ZHAO Yan-shuang, YANG Tian-yan, XIAO Pei-tao, ZHENG Chun-man. Cathode electrolyte interface engineering by gradient fluorination for high-performance lithium rich cathode [J]. Advanced Energy Materials, 2023, 13: 2301765.

[52] BAI Pan-xing, JI Xiao, ZHANG Jia-xun, ZHANG Wei-ran, HOU S, SU Hai, LI Meng-jie, DENG Tao, CAO Long-sheng, LIU Su-fu, HE Xin-zi, XU Yun-hua, WANG Chun-sheng. Formation of LiF-rich cathode−electrolyte interphase by electrolyte reduction [J]. Angewandte Chemie International Edition, 2022, 61: e202202731.

通过超薄 ZrO_2 表面涂层提高尖晶石 $LiNi_{0.5}Mn_{1.5}O_4$ 正极材料的长循环稳定性

梅 洁[1,2]，徐启翔[1,2]，陈远志[1,2]，高贵阳[1,2]，徐万杰[1,2]，谢清水[1,2]，王来森[1,2]，彭栋梁[1,2]

1. 厦门大学 材料学院 固体表面物理化学全国重点实验室，厦门 361005；
2. 厦门大学 福建省高性能材料表面与界面工程重点实验室，厦门 361005

摘 要：尖晶石 $LiNi_{0.5}Mn_{1.5}O_4$ (LNMO)正极材料由于其独特的电压平台，在储能领域受到了极大的关注。为了进一步提高 LNMO 的长循环稳定性，通过原子层沉积(ALD)技术制备了超薄 ZrO_2 层包覆的 LNMO 正极材料。结果表明，沉积 20 层 ZrO_2 包覆层的 LNMO (LNMOZ20)正极材料表现出最佳的电化学性能。在 1*C* 的电流密度下，LNMOZ20 的放电容量高达 117.1 mA·h/g，循环 600 周后的容量保持率为 87.4%。此外，即使在 5*C* 和 10*C* 的更高电流密度下，LNMOZ20 电极也表现出优异的稳定性，其放电容量分别为 111.7 和 103.6 mA·h/g，循环 2000 周后的容量保持率分别为 81.0%和 101.4%。本研究表明，在 LNMO 正极材料表面通过 ALD 沉积超薄 ZrO_2 包覆层是一种提高其长循环稳定性的有效策略。

关键词：尖晶石 $LiNi_{0.5}Mn_{1.5}O_4$；ZrO_2 涂层；高压正极；原子层沉积；正极电解质界面膜

(Edited by Wei-ping CHEN)